Applied Surface Science 622 (2023) 156908

Contents lists available at ScienceDirect

Applied Surface Science

journal homepage: www.elsevier.com/locate/apsusc

Full Length Article

Laser-induced periodic surface structuring for secondary electron yield reduction of copper: dependence on ambient gas and wavelength

Jijil JJ. Nivas [a,b,c], Meilin Hu [b], Mohammadhassan Valadan [a,d], Marcella Salvatore [b,e], Rosalba Fittipaldi [a,f], Marcel Himmerlich [g], Elena Bez [g,h], Martino Rimoldi [g], Andrea Passarelli [a], Stefano L. Oscurato [b], Antonio Vecchione [f], Carlo Altucci [a,d], Salvatore Amoruso [a,b,c], Antonello Andreone [a,b,c], Sergio Calatroni [g], Maria Rosaria Masullo [a,*]

[a] Istituto Nazionale di Fisica Nucleare, Sezione di Napoli, Complesso Universitario Monte S. Angelo, Via Cinthia, I-80126 Napoli, Italy
[b] Dipartimento di Fisica "Ettore Pancini", Università degli Studi di Napoli Federico II, Complesso Universitario Monte S. Angelo, Via Cinthia, I-80126 Napoli, Italy
[c] CNR-SPIN, UOS Napoli, Complesso Universitario Monte S. Angelo, Via Cinthia, I-80126 Napoli, Italy
[d] Dipartimento di Scienze Biomediche Avanzate, Università degli Studi di Napoli Federico II, via Pansini 5, I-80131 Napoli, Italy
[e] Centro Servizi Metrologici e tecnologici Avanzati (CeSMA), University of Naples "Federico II", Complesso Universitario San Giovanni, Corso Nicolangelo Protopisani, Naples, Italy
[f] CNR-SPIN, UOS Salerno, Via Giovanni Paolo II 132, I-84084 Fisciano, Italy
[g] CERN, European Organization for Nuclear Research, 1211, Geneva 23, Switzerland
[h] Faculty of Physics and Earth Sciences, University of Leipzig, Linnéstraße 5, 04103 Leipzig, Germany

ARTICLE INFO

Keywords:
Laser induced periodic surface structures
Surface roughness
Secondary electron emission
Particle accelerator physics

ABSTRACT

One of the main limitations for future high-performance accelerators operating with positively charged particles is the formation of an electron-cloud inside the beam vacuum chamber, giving rise to instabilities. The Secondary Electron Yield (SEY) of the beam-facing surfaces gives a measure of the mechanism which drives this phenomenon. The laser-induced periodic structure formation on Cu surfaces has been demonstrated as a promising process to reduce SEY. In view of applications in beam chambers, we studied the laser process influence on SEY for 515 and 1030 nm wavelength femtosecond pulses on copper in different ambiences (air, nitrogen, vacuum). Depending on used process conditions, the surface composition differs, structures with varying aspect ratio are formed, i.e., periodic ripples and large-scale channels. Treatment in air at 515 nm is the most efficient for the formation of deeper structures allowing SEY maximum reduction first down to 1.6–1.7 and then below unity upon electron irradiation, thereby totally suppressing electron-cloud. Increasing the laser fluence, SEY will further reduce due to surface roughness enhancement via nanoparticle redeposition. This study reveals the fundamental role of LIPSS treatments to enable surface treatment in large-scale accelerator installations, where particle-free components are desired, and paves the way to potential future applications.

1. Introduction

The performance of particle accelerators is influenced by the interaction of circulating beam and emitted synchrotron radiation with the residual gas molecules in the vacuum system as well as with the beam pipe walls. Among the possible phenomena inside the accelerator vacuum chamber, the circulating beam can produce primary electrons, via ionization or photoemission, and subsequently accelerate them up to energies of several hundred electronvolt. When accelerated, the primary electrons can hit the chamber walls producing secondary electrons that if survive will multiply in an avalanche effect [1], during the passage of the following particle bunches: the e-cloud is formed. The probability of secondary electrons' production and their survival strongly depend on the wall surface characteristics. The emission of secondary electrons can be described resorting to the Secondary Electron Yield (SEY) of the metallic vacuum pipe surface. The SEY, defined as the ratio between the number of secondary electrons emitted from a surface and the number of incident electrons, depends on the energy of the primary electrons hitting the surface. If the SEY of the vacuum chamber surface is significantly larger than unity, an avalanche multiplication process will be

* Corresponding author.
E-mail address: masullo@na.infn.it (M. Rosaria Masullo).

https://doi.org/10.1016/j.apsusc.2023.156908
Received 3 January 2023; Received in revised form 17 February 2023; Accepted 27 February 2023
Available online 2 March 2023

induced and the electron density will rapidly increase. The resulting e-cloud will limit the accelerator performance causing beam instabilities or degradation [2,3] and local detrimental phenomena, such as heat load to cryogenic system via warm-up of beam pipe walls, and pressure rises [4].

Electron-cloud formation is one of the primary issues in high-energy colliders, storage and damping rings, operating with positively charged particles [5], consequently, mitigation of its impact is a crucial research topic in particle accelerator physics.

Among different strategies for electron cloud mitigation, SEY reduction of accelerator component metal surfaces is the most implemented. Ideally, a material should be used with intrinsically low and stable SEY and compatible with all vacuum and impedance requirements, as in the case of pure metal surfaces. Alternatives to the use of bulk materials that fulfil the mentioned criteria are either the application of functional coatings based on amorphous carbon [6] or non-evaporable getter (NEG) [7] films or/and a geometrical modification of the surface [8,9].

The ability of laser surface micromachining in reducing SEY has been already investigated in the past: laser engineered surface structures (LESS), created by nanosecond or femtosecond pulsed laser irradiation effectively reduced the SEY, affecting the survival probability of secondary electrons and optical absorbance of metal surfaces [10–15]. However, femtosecond laser induced periodic surface structures (LIPSS) showcase advantages over the other alternatives [16]. Even though the SEY is higher, particle-free surfaces can be created. Femtosecond laser micromachining of solid surfaces allows the direct writing of periodic surface features at a scale varying from below wavelength to millimeters, including hierarchical surface structuring, without demanding any expensive or multistage fabrication process [17]. As a consequence, this technique offers a powerful method to fabricate functional surfaces with very peculiar properties, spanning from the modification of optical properties to the enhancement or switching of the wettability [18–20]. The generated surface microstructures greatly depend on experimental parameters, such as laser wavelength, polarization, energy and number of pulses, repetition rate, scan velocity [17,21–25]. The significant role of femtosecond LIPSS on a copper surface with subwavelength-sized features on the SEY is demonstrated in our previous study, in which the role of laser polarization on the surface treatment was addressed [16]. The SEY is also fundamentally influenced by the material surface chemical composition. As a consequence, the background gas and its pressure during processing have great impact on the final textured surface and its properties: reducing the gas pressure lowers the number of redeposited nanoparticles [26], while a low-oxygen content environment at atmospheric background pressure (such as nitrogen) can suppress potential detrimental oxidation effects [11].

Meanwhile the LIPSS technique has some advantages, the feasibility of its implementation in a real accelerator on long distances of the order of several hundreds of meters is still to be demonstrated. For these reasons, in the present work we investigate the influence of three processing parameters, laser wavelength, beam scanning velocity and ambient gas, on SEY of laser-structured copper and correlate these parameters with the induced morphological and compositional modifications at the surface. Oxygen-free electronic grade copper used is one of the most commonly used vacuum pipe materials. These studies open a perspective for tailored laser-based treatments of metal surfaces and settle a new solid protocol for texturing surfaces and interfaces in view of fundamental applications such as those to particle accelerator physics.

Furthermore, any coating or surface functionalization technology applied on vacuum pipes for e-cloud mitigation alters the surface impedance potentially leading to undesired beam instabilities. The estimation of the surface resistance under operating conditions is fundamental to develop valid models of the beam-machine impedance and to identify limits in the accelerator performances. Therefore, studying the electromagnetic (EM) response of these modified copper surfaces [27–29], influenced by their resistivity, thickness and roughness, is of particular interest. In this paper we also report preliminary studies of the impact of LIPSS on the copper surface impedance, by measuring the sample conductivity at 15 GHz. The LIPSS-induced changes of SEY and surface conductivity are evaluated in comparison to a pristine copper.

2. Experimental methods

2.1. Sample preparation.

Surface processing of copper samples was carried out using a chirped pulse amplification Yb:KGW laser system delivering pulses with a duration of ≈ 180 fs with the fundamental wavelength of λ ≈ 1030 nm. The laser was a modified Light Conversion Pharos H1-SP-1.5 mJ system, equipped with a pulse selector that allows defining a sequence of *N* laser pulses with any value of the repetition rate up to that of the Regenerative Amplifier (RA). The laser source is equipped with an external, free-standing harmonic generator (HIRO, Light Conversion) providing pulses at the second harmonic (λ ≈ 515 nm) through a generation in a BBO crystal and subsequent wavelength filtering. Copper was selected as the target material by considering its relevance and utilization in high-energy particle accelerators such as the Large Hadron Collider (LHC) at CERN [30]. The laser beam was focused onto the sample using a lens with a nominal focal length of 200 mm at normal incidence. Before focusing, the beam was passed through a variable aperture to select the intense part of the beam and then through a half wave plate to adjust the polarization along scanning direction. In this experiment, the laser was operated at a repetition rate of $f_p = 5$ kHz. The target was mounted on a computer-controlled XY-translation stage (PP-20, Micronix USA) that was synchronized with the laser. A block diagram of experimental setup is provided in Fig. 1.

The spot radius of the Gaussian laser beam on the target surface was attained in both irradiation wavelength by following the methods proposed by Liu [31–33] and also supported by theoretical conclusions for the case of fs irradiation [34]. The estimated beam radius w_0 and the corresponding threshold fluence F_{th} values are reported in Table 1. The peak fluence for the Gaussian beam can be calculated using $F_p = (2E)/(\pi w_0^2)$ with E being the pulse energy. Polycrystalline oxygen-free electronic grade (OFE – purity > 99.99%) copper plates of 1 mm thickness were cut into 20 × 20 mm^2 large samples and subsequently underwent a standard procedure for UHV cleaning including a wet-chemical detergent-based degreasing process followed by rinsing in deionized water and storage in air in silk paper after drying. Laser processing was performed several weeks after the cleaning procedure. The experiments were carried out at both wavelengths (1030 and 515 nm) in three different ambient conditions: ambient air, rough vacuum ($p \approx 4 \times 10^{-3}$ mbar) and nitrogen at 1000 mbar in the same experimental setup. Subwavelength ripples with orientation perpendicular to the polarization are formed because of fs pulse irradiation. On each copper sample, three segments of 8 × 8 mm^2 were processed implementing continuous bidirectional raster scanning of the laser beam along the horizontal direction together with a line separation Δ along the vertical direction, also called hatch distance. Further laser processing parameters are reported in Table 1. In all cases, the scanning direction was set parallel to laser polarization direction. Three selected velocities $v = 1$, 1.5, and 2 mm/s were employed, defining the effective number of overlapping pulses $N_{eff} = \left(2w_0 f_p\right)/v)$ [35]. Thus, the pulse overlap $(1 - \frac{1}{N_{eff}})$ is for all cases >99 %.

2.2. Material characterization

After processing, the samples were stored in wafer boxes and shipped to CERN. Their surfaces were then characterized in ultra-high vacuum by secondary electron yield (SEY) measurements as well as X-ray

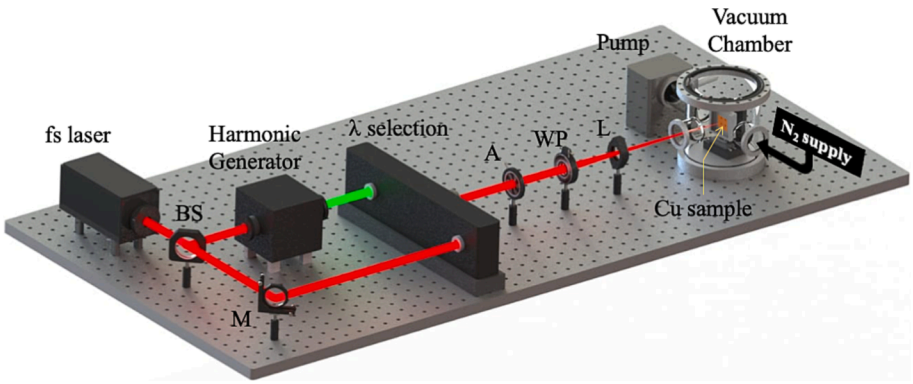

Fig. 1. A simple block diagram of the experimental setup used for the surface structuring of Cu in different ambience at two wavelengths with the following components: BS- a 50/50 beam splitter, M-ultrafast mirror, A-variable aperture, WP-half wave plate, L-focusing lens. Inside the vacuum chamber, the Cu sample is fixed on a high precision two axis stage which is controlled by means of a custom software. A vacuum pump is used to pump down the pressure inside the chamber and external gas supply is used to fill up the chamber in case of processing in nitrogen. The box marked as λ-selection represents the possibility to select either the fundamental output of the laser (1030 nm) or its second harmonic (515 nm).

Table 1
Laser processing parameters (E – pulse energy, Δ – hatch distance, w_0 – Gaussian spot radius, F_{th} – ablation threshold).

λ (nm)	E (μJ)	Δ (μm)	w_0 (μm)	F_{th} (J/cm^2)
515	16	30	35	0.14 ± 0.04
1030	84	40	91	0.24 ± 0.03

photoelectron spectroscopy (XPS) and electron-irradiation tests according to the experimental procedures described in [16]. Subsequently, the surface morphology of the laser-treated copper samples was studied by Optical Microscopy, Scanning Electron Microscopy (Zeiss Leo EVO 50), and Atomic Force Microscopy in combination with Raman spectroscopy (WITec Alpha 300 RAS, λ = 488 nm), allowing a larger material probing depth compared to the XPS analyses.

For the EM characterization of surface resistance, not all the measurement methods are equivalent. Especially in the case of very thin and low-loss coating materials or if the surface modification is limited to a very thin surface region with an expected conductivity close to the bulk value (as in the case of LIPSS), standard broadband methods such as transmission or reflection techniques in time- or in frequency-domain [36] do not offer sufficient sensitivity. Considering the corresponding surface modulation, the change in conductivity in LIPSS is expected to be even lower than in LESS samples. We therefore applied a resonant perturbative technique, which is inherently limited to a very narrow frequency range. The method is based on the measurement of the change in the quality factor of a dielectrically loaded copper cavity [37–39], measured in our case at ~ 15 GHz with a Vector Network Analyzer (Rohde & Schwarz ZNB 20), and is accurate for determining the conductivity of very thin samples (roughness or film thickness < 3 μm) [37,38].

3. Results and discussion

3.1. Morphological analysis.

A simple schematic of laser processing with bidirectional scanning is shown in Fig. 2 (a). For the treatment parameters implemented in this study, this process generates two typical modulations on the irradiated surface [13]: *i)* subwavelength-wide ripples of periodicity Λ with preferential alignment perpendicular to the laser polarization and *ii)* large-range topography modulation ('channels') along the scanning direction generated because of material ablation, that are dependent on the Gaussian intensity profile of the focused laser spot and have a periodicity equal to Δ. An optical micrograph of the copper surface after irradiating the sample with 515 nm fs pulses at $v = 1$ mm/s is shown in Fig. 2 (b) and highlights the large-scale modulation of the surface topography. To evaluate the change in the surface morphology on smaller scale, SEM and AFM of untreated and laser-treated copper surfaces were performed. The original OFE Cu surface is rough with micrometer-sized non-uniformities (Fig. 2 (c), (f)) originating from the rolling process during fabrication. The micrographs in (d), (e), (g) and (h) correspond to samples treated in air at $v = 1$ mm/s. The Cu surfaces processed with λ ≈ 515 nm and 1030 nm laser light exhibit periodic ripples (LIPSS) with an average spatial period of Λ = 332 ± 22 nm and Λ = 697 ± 65 nm, respectively. The related AFM images clearly prove the presence of sub-

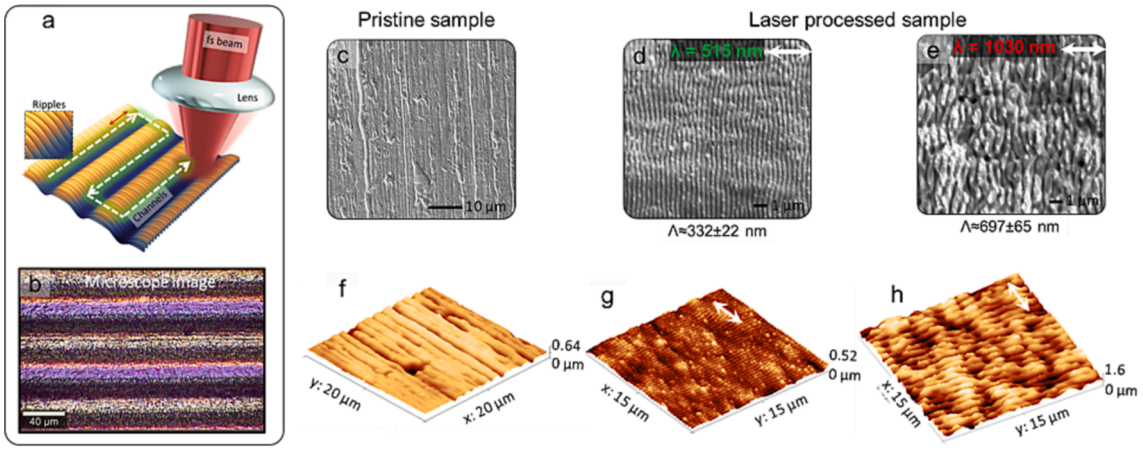

Fig. 2. (a) Graphical representation of the structural surface changes induced by the implemented laser treatment, (b) optical micrograph of a Cu sample processed at v = 1 mm/s with 515 nm fs pulses. SEM images of the copper surface before laser processing (c), after irradiation in ambient air and v = 1 mm/s with at 515 nm (d) and 1030 nm (e). AFM (3D view) images of the copper surface before (f) and after laser processing at 515 nm (g) and 1030 nm (h). The white double-headed arrows indicate the direction of laser polarization.

micron periodic ripples, whose spatial period depends on the irradiation laser wavelength. The related AFM images clearly prove the presence of sub-micron periodic ripples, whose spatial period depends on the irradiation laser wavelength. The surface topography characterization was performed by means of AFM operated in tapping mode. To avoid underestimation of depth values, we used high-aspect-ratio probes (aspect ratio $>$ 5:1, radius $<$ 10 nm, half cone angle $<$ 5°) mounted on a cantilever with resonance frequency 75 kHz.

The influence of λ, *v*, and of the surrounding atmosphere was further analyzed, while all other processing parameters (pulse energy, repetition rate and spot size, see Table 1) were kept constant. Fig. 3 includes SEM images at identical magnification of sample surfaces for laser processing at λ ≈ 515 nm and 1030 nm at$v$ = 1.5 mm/s in ambient air, rough vacuum, or nitrogen. In all three environments, well-defined ripples were formed, while in addition particles are detected at the surface after treatment in air, and in a lower quantity for treatment in nitrogen. In the case of processing in vacuum, the surface is almost free of nanoparticles. However, the ripple surface exhibits a nanoscale roughness. This could be due to the nature of the ablation process itself, as shown by two-temperature-model simulations and molecular dynamics simulations by Wu and Zhigilei [40], which involved melting and resolidification of part of the material with subsequent freezing of nanosized features on the target surface after the ablation process. Such dynamics can depend on the material characteristics which can make the surface of the ripples comparatively rougher for copper when compared to the smoother ones formed on other materials, like in the case of Si, after processing under reduced pressure [26]. The presence of nanoparticles on the structured surface can be ascribed to redeposition, which is an obvious phenomenon in the case of fs laser ablation at ambient pressure as the expanding plasma plume is confined by the surrounding gas pressure. In that sense, the nanoparticle-free ripples observed after treatment in vacuum are a result of the complete escape of ablated material from the copper surface. Furthermore, in the case of processing in vacuum and nitrogen, the ripples seem to be shallow compared to processing in air. Moreover, the SEM data evidence the existence of random modulations on the surface, which could be due to the surface nonuniformities present on the original sample. The ripples appear to be generated over this rough surface. Nonetheless, the pre-existing surface modulations from the fabrication process visible on the pristine copper samples will also exist on real accelerator components.

In the case of irradiation at λ ≈ 1030 nm, SEM images reveal sample surfaces that in all three ambient conditions are rather free from nanoparticulate debris (see supplementary information, Figs. S1 and S2, for SEM images after processing at 515 nm and 1030 nm).

Fig. 4(a-f) reports high-resolution AFM images of the ripples obtained after irradiating with λ ≈ 515 nm and 1030 nm in the three different ambient conditions at v = 1.5 mm/s. In all cases, the images

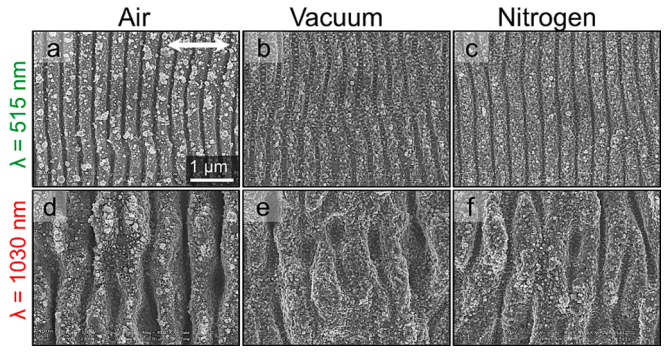

Fig. 3. SEM images of LIPSS generated with two different laser wavelengths (515 and 1030 nm) in three different environments (air, vacuum, and nitrogen ambience) at v = 1.5 mm/s. The white double-headed arrow in (a) indicates the laser beam polarization direction.

evidence the presence of surface ripples. Fig. 4 (g) includes extracted line profiles as a function of v for the processing in air at 515 nm. No clear evidence of variations in dependence of scanning speed is visible (see supplementary information, Figs. S3, S4 and S5, for AFM images after processing at 515 nm and 1030 nm in the three different ambient conditions and at three beam scanning velocities).

The large-area AFM image in Fig. 5 (a) of a copper sample, that was processed in air at 1 mm/s and with λ ≈ 515, shows the large-scale periodic modulation generated along the scanning direction. The inset shown in Fig. 5 (a) displays the 3D view of the processed surface with valley and peak of the formed channels. For all the samples the beam scanning direction was parallel to the laser polarization. Therefore, the formed ripples and channels are orthogonal to each other.

The AFM line profiles for the case of λ ≈ 515 nm reported in Fig. 5 (b) and (c), exemplify the shape of the large-scale channels as a function of the scanning velocity and of the ambient condition during treatment. It can be concluded from Fig. 5 (b) that the channels are very shallow when the irradiation is carried out in vacuum or in nitrogen ambience, even though the laser parameters are identical to those of irradiation in air. This behavior suggests a comparatively reduced ablation and material removal when the laser treatment was carried out in vacuum or in nitrogen. Previous experimental findings show that in the case of silicon, with a 35–45% increase of the threshold fluence value, the switching from air to vacuum is likely associated with the differences in surface morphology and composition in the two cases [26]. Due to a progressive decoration with nanoparticles, the target surface in air develops a rougher and grainier texture than it does in vacuum. According to previous studies, multi-pulse ultrashort laser irradiation of target surfaces densely decorated with nanoparticles and nanostructures gradually alters their absorption properties, eventually leading to colored or blackened surfaces [18,41]. However, in nitrogen ambience even though the pressure is set to 1000 mbar the surface shows a reduced material removal.

In addition, we anticipate that processing in air and vacuum induce different changes in the chemical composition of the irradiated surface, especially with respect to the modification of surface oxide and adsorbate layers, that can possibly affect the energy coupling to the target, thus resulting in the observed differences in the ablation efficiency. This aspect will deserve further investigations in the future to fully clarify it. Consequently, a clear change in the channel depth could only be measured for the samples processed in air. Fig. 5 (c) includes the change of the channel profile for treatment at 515 nm in air. As the beam scanning velocity reduces from 2 to 1 mm/s, there is a clear increase in the peak-to-valley height or channel depth 'd_C' from 0.38 to 1.1 μm. The spatial periodicity of the surface ripples Λ was measured both by SEM and AFM for all samples. In Table 2 the values obtained from SEM analyses are summarized for the different ambient conditions and scanning speeds and agree with those obtained from AFM. No variation of Λ has been measured when changing the scanning speed or the ambient conditions, whereas this parameter strongly depends on the laser wavelength.

The depth profiles of the coarser channels d_C, reported in Fig. 5 (b) and (c), have been determined from AFM measurements and the depth values are summarized in Table 2. Moreover, the depth of the ripples was estimated by measuring the value of peak-to-valley height of ripples d_R at any selected local area from the AFM data using the Gwyddion software.

The aspect ratios of these two surface modulations (channels and ripples) can be estimated separately by taking the ratio of the peak-to-valley height and the corresponding spatial period. For the channels, the aspect ratio was evaluated as d_C /Δ, while for the ripples the aspect ratio is defined as d_R /Λ. The estimated values for channels as a function of laser wavelength and scanning velocity are reported in Fig. 5 (d) only for processing in air, because no channels were created in the case of vacuum or nitrogen ambience.

A clear drop in the aspect ratio of the channels can be observed as the

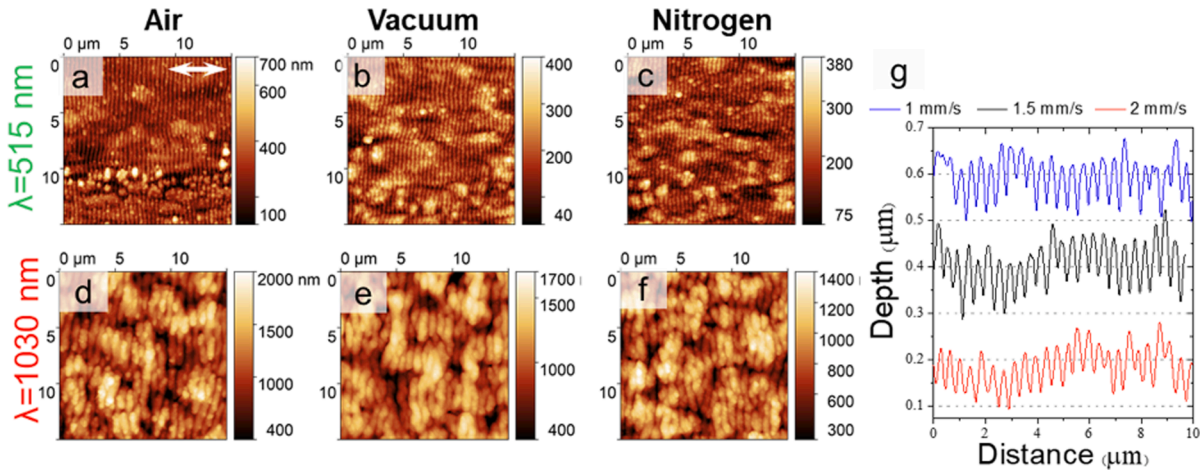

Fig. 4. (a-f) High-resolution AFM images of the surface after processing with 515 nm (a-c) and 1030 nm (d-f) at v = 1.5 mm/s for three ambient conditions. The white double-headed arrow in (a) indicates the incident laser light polarization direction. (g) Depth profile of surface ripples at three scanning velocities generated in air at λ ≈515 nm. The profiles are vertically shifted for the sake of clarity.

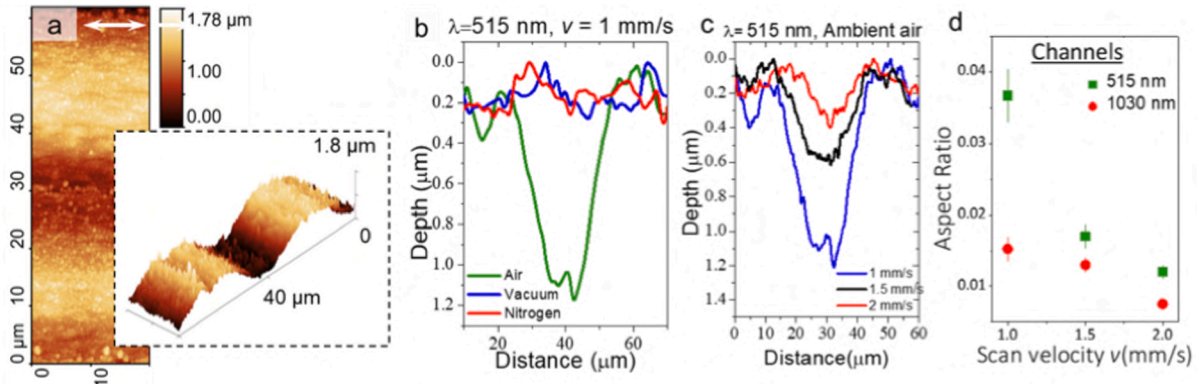

Fig. 5. (a) Low-resolution AFM image after processing with λ ≈ 515 nm in ambient air at v = 1 mm/s to showcase the surface waviness due to the large-scale modulation called channels. The inset in (a) represents the 3D view of the large-scale surface modulation. The channel depth profiles are reported in (b) and (c) as a function of the ambient conditions and of the scanning speed, respectively. Panel (d) shows the aspect ratio of channels as a function of scanning velocity for irradiation at 515 and 1030 nm in ambient air.

Table 2
Spatial period Λ of ripples, depth of large-scale channels d_C and peak-to-valley height of ripples d_R generated at copper surfaces during irradiation with fs laser pulses at 515 and 1030 nm. The surface roughness due to the sub-wavelength ripples were extracted from the AFM measurements by obtaining an average value of peak-to-valley of ripples d_R using the Gwyddion software.

λ (nm)	v(mm/s)	Λ (nm)			d_C (μm)	d_R (nm)		
		Air	Vacuum	Nitrogen	Air	Air	Vacuum	Nitrogen
515	**1**	350 ± 24	364 ± 34	332 ± 27	1.1 ± 0.05	83 ± 10	43 ± 6	49 ± 5
	1.5	341 ± 23	375 ± 24	361 ± 25	0.51 ± 0.02	73 ± 6	49 ± 6	41 ± 4
	2	344 ± 20	389 ± 23	384 ± 29	0.36 ± 0.02	48 ± 5	48 ± 4	42 ± 4
1030	**1**	697 ± 65	647 ± 49	622 ± 66	0.61 ± 0.03	334 ± 19	202 ± 10	218 ± 17
	1.5	785 ± 50	678 ± 47	669 ± 68	0.52 ± 0.04	262 ± 21	219 ± 8	172 ± 17
	2	809 ± 42	707 ± 43	674 ± 59	0.30 ± 0.03	185 ± 11	259 ± 18	181 ± 11

scanning velocity increases, especially for λ ≈ 515 nm. Table 3 includes the calculated aspect ratios of the ripples, for which a decrease is found when processing in air and increasing the scan velocity from 1 to 2 mm/s. For the other two ambiences (vacuum and nitrogen) and for both wavelengths, the values are lower than those for treatment in air, while no significant differences are observed for variation of the scan speed in this case. In general, the ripple aspect ratio is higher for 1030 nm treatment, which is linked to significantly deeper ripple structures in this case, while the lateral period is larger by a factor of two.

3.2. *Spectroscopic characterization: XPS and Raman analyses.*

XPS analyses were carried out to investigate the chemical composition of the surface after fs laser processing on the samples treated at a scan velocity $v = 1.5$ mm/s in the different environments (ambient air, vacuum, nitrogen) and for the two laser wavelengths (515 nm and 1030 nm). Fig. 6(a) includes the Cu 2p, Cu LMM, O 1s and N 1s spectra only for λ ≈ 515 nm. The spectra for the samples processed with 1030 nm light exhibit the same characteristics and trends. The resulting surface composition is dependent on the chosen gas environment during laser

Table 3
Aspect ratio of the ripples generated on copper after irradiating with laser pulses at λ ≈ 515 nm and 1030 nm in air, vacuum, and nitrogen for different scanning speeds.

Velocity (mm/s)	Aspect Ratio of ripples					
	515 nm			1030 nm		
	Air	Vacuum	Nitrogen	Air	Vacuum	Nitrogen
1	0.24 ± 0.03	0.11 ± 0.02	0.15 ± 0.03	0.44 ± 0.05	0.32 ± 0.04	0.28 ± 0.04
1.5	0.21 ± 0.02	0.13 ± 0.02	0.11 ± 0.02	0.33 ± 0.03	0.28 ± 0.03	0.23 ± 0.03
2	0.14 ± 0.02	0.14 ± 0.02	0.11 ± 0.02	0.24 ± 0.02	0.32 ± 0.03	0.23 ± 0.03

processing. Most relevant, the laser structuring performed in air resulted in a higher oxygen content at the surface, compared to the treatments in oxygen-free environment (vacuum and nitrogen) (see surface composition in the supplementary information, Table S1 and the XPS spectra of a degreased Cu sample prior to laser processing, Fig. S6).

The surface after processing in air has a major component of Cu_2O as the binding energy (BE) of the Cu $2p_{3/2}$ state is at 932.3 eV and the Cu LMM Auger peak is at a kinetic energy of 916.8 eV (modified Auger parameter of 1849.1 eV) [42–44]. In addition, the Cu $2p_{3/2}$ side state at 934.5 eV BE, the related spectral fingerprint of the satellite features between 940 and 948 eV, and the enhanced O 1s peak at 531.5 eV for treatment in air indicate the presence of copper hydroxide bonds [44]. Important to note is that, considering the surface sensitivity and the related detection limits of the XPS analyses, no significant formation of detrimental surface CuO [45] took place during LIPSS formation. In contrast, for treatments in air at higher laser power and fluence, the redeposition of oxidized CuO nanoparticles from the generated plasma plume typically occurs[46], which charge up when exposed to electrons or positive ions in UHV at cryogenic conditions [12]. In all XPS analyses on the surfaces with LIPSS, including the sample treated in air, CuO traces, if any, remain at the edge of identification limit and would neither influence the SEY nor lead to critical surface charging at low temperatures.

After treatment under rough vacuum conditions or in nitrogen, the surface compositions differ. Besides the presence of a Cu_2O phase, a portion of the near-surface copper atoms is in metallic state (Cu^0), as indicated by the additional peak in the Cu LMM Auger electron emission (KE of 918.4 eV and modified Auger parameter of 1850.8 eV). The surface oxygen and hydroxide contents are lower as well. Both effects are more distinct when the processing was performed in vacuum. One must consider that the ablation processing in oxygen- and residual water-free environment will initially create a rather clean and reactive surface, free of hydroxides and with low degree of oxidation. Nonetheless, since pure copper is a reactive material, the exposure to ambient conditions will lead to further reactions and ageing, as it was partially the case for the subsequent sample transfer and material analysis in this study and will be the case for installation of components into any experimental equipment [47–49]. Furthermore, the treatment in N_2 induces the incorporation of nitrogen at the surface at a level of 2–3 at. % (see N 1s state at 397.3 eV in Fig. 6(a)). This trend had already been observed earlier when processing Cu surfaces in N_2 with a picosecond laser operating at 532 nm [12]. The incorporation of additional elements can affect the reactivity of the surface as well as its affinity to adsorption of species from the ambient.

Further investigations on the chemical composition of the samples processed in different ambient conditions and with different wavelengths have been performed by Raman spectroscopy and compared

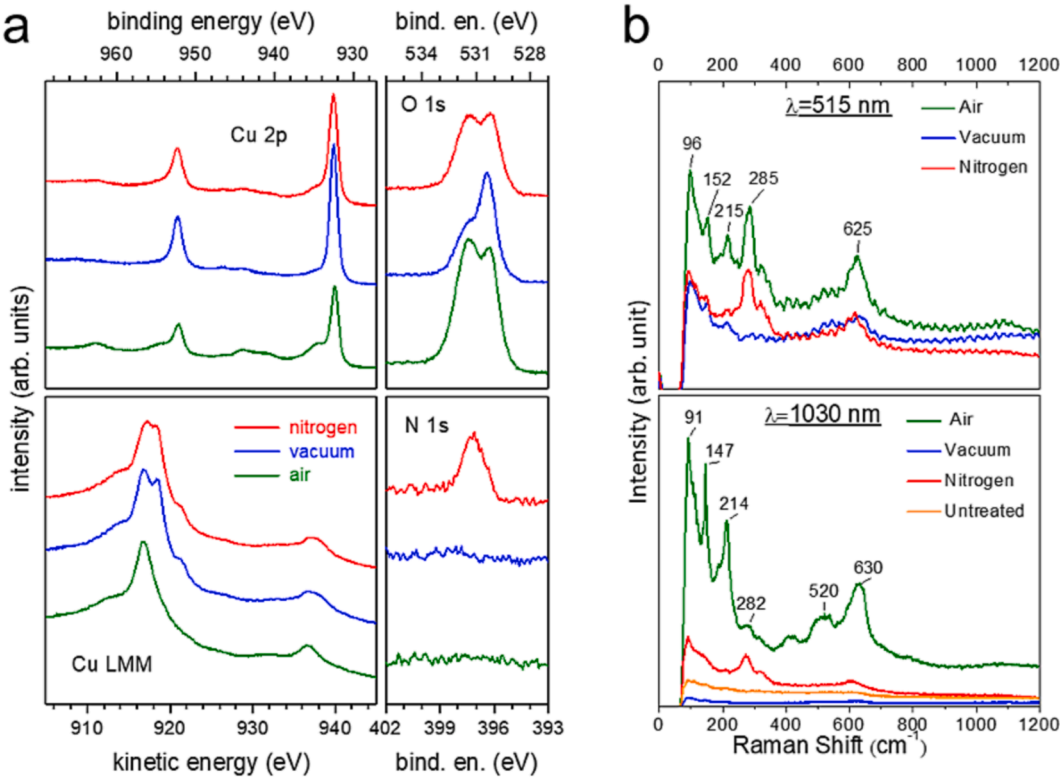

Fig. 6. (a) XPS spectra (Cu 2p, Cu LMM, O 1s, and N 1s) of Cu samples after treatment with 515 nm laser light at a scanning speed of 1.5 mm/s in nitrogen (red), vacuum (blue), or ambient air (green). (b) Raman spectra acquired for samples processed at 515 nm (top) and 1030 nm (bottom) at a scanning velocity of 1.5 mm/s for the different ambient conditions. These spectra represent an average of 50 individual measurements each. (For interpretation of the references to colour in this figure legend, the reader is referred to the web version of this article.)

with that of pristine copper. The corresponding spectra are shown in Fig. 6(b). The results for the samples processed at $v = 1.5$ mm/s are selected as a representative case. The samples processed in air at both wavelengths exhibit the series of Raman peaks at 91, 142, 214, 520, and 629 cm^{-1} that identify Cu_2O, corroborating its prevalence on the air-processed surface. Moreover, the additional broad band between 400 and 600 cm^{-1} in the case of the sample processed in air at 1030 nm may indicate a phase change or a large number of structural defects in the crystalline lattice [50]. Samples processed in nitrogen did not show considerable oxidation in the Raman spectra, suggesting a contribution of the ambient oxygen gas on the chemical features of the samples processed in air. After processing in air or N_2, an additional peak is detected around 282–285 cm^{-1}. Cupric oxide single crystals exhibit Raman signatures at 298, 345 and 632 cm^{-1} at room temperature [51] and in literature a clear assignment of these peaks to CuO Raman modes is found. However, since the reported peak positions may vary considerably, the detected peak might possibly indicate the presence of CuO nanocrystals on the processed surface in the case of laser treatment in ambient air and nitrogen [52].

Nevertheless, the absence of clear CuO signatures in the XPS results makes such hypothesis unfavorable. In this respect, it is worth noticing that due to intrinsic defects and non-stoichiometry [53] also Raman spectra of Cu_2O can vary significantly in the number of observed modes and their relative intensities with respect to those of a single crystal. Surely this can be the case for the laser-irradiated copper investigated here. For instance, peaks at positions close to those pertaining to a CuO single crystal can also be expected in the Raman modes of Cu_4O_3 (Paramelaconite) according to analyses of samples prepared by RF magnetron sputtering [54]. However, the authors of this study pointed out that a clear assignment of the observed Raman peaks cannot be reliably made, since the strong signals could also be ascribed to nominally forbidden or multi-phonon Raman modes of Cu_2O. All these aspects point out the difficulty in assigning Raman mode in non-perfect material and highlight to utilize complementary spectroscopic techniques for material analysis.

The treatment in vacuum induced only a minor change to the sample composition as accessible by Raman spectroscopy, further highlighting a more significant chemical modification of the surface in air compared to structuring in vacuum or nitrogen. Ultimately, the spectra confirmed the XPS findings regarding the oxide content on the processed surface, being maximum for treatment performed in air, and clearly show that the processing in vacuum suppressed the oxide content, within the limit of the Raman sensitivity.

3.3. Secondary electron yield characterization

The dependence of the SEY on the primary electron energy for Cu samples processed with 515 and 1030 nm laser light in different ambiences and at different scanning speed are shown in Fig. 7. The extracted maxima of these curves are summarized in Table 4. The values for untreated Cu after detergent cleaning typically range from 1.9 to 2.2 depending on the amount of adsorbates and related storage conditions [55,56]. The most evident reduction of the SEY and its maximum δ_{max} compared to untreated air-exposed Cu was found for the samples treated in air, achieving a δ_{max} of 1.61 at 800 eV and 1.74 at 600 eV for 515 nm and 1030 nm photons, respectively. The treatments in vacuum or nitrogen induced only marginal changes with δ_{max} ranging from 1.99 to 2.27.

Furthermore, samples processed in air exhibit a common trend at both wavelengths: as the scanning velocity is lowered from 2 to 1 mm/s, a decrease in δ_{max} is evident. At lower scanning velocity a larger number of pulses overlap, which results in a higher accumulated fluence. This clearly influenced the ripple depth, d_R, that almost doubled from 2 mm/s to 1 mm/s (see Table 2), together with interlinked properties such as the ripple depth and the aspect ratio that characterize the geometry of the periodic features. It is worth to note that inherent redeposited nanoparticles as well as other debris also show an increased presence at lower scanning speeds. In addition, the scanning speed also influenced the depth of the large-scale channels formed via direct material ablation induced by the scanning laser spot with Gaussian intensity profile (see

Table 4
Secondary electron yield maximum δ_{max} and the corresponding primary electron energy $E(\delta_{max})$ after laser irradiation in air, vacuum, and nitrogen at scanning velocities of 1, 1.5, and 2 mm/s using different wavelengths (515 and 1030 nm).

λ (nm)	ν(mm/s)	δ_{max} / $E(\delta_{max})$ (eV)		
		Air	Vacuum	Nitrogen
515	2	1.89 / 450	2.07 / 400	2.14 / 400
	1.5	1.77 / 600	2.05 / 400	2.11 / 400
	1	1.61 / 800	2.01 / 400	2.27 / 400
1030	2	1.88 / 600	2.03 / 400	1.99 / 400
	1.5	1.79 / 500	2.06 / 400	2.02 / 400
	1	1.74 / 600	2.07 / 375	2.01 / 450

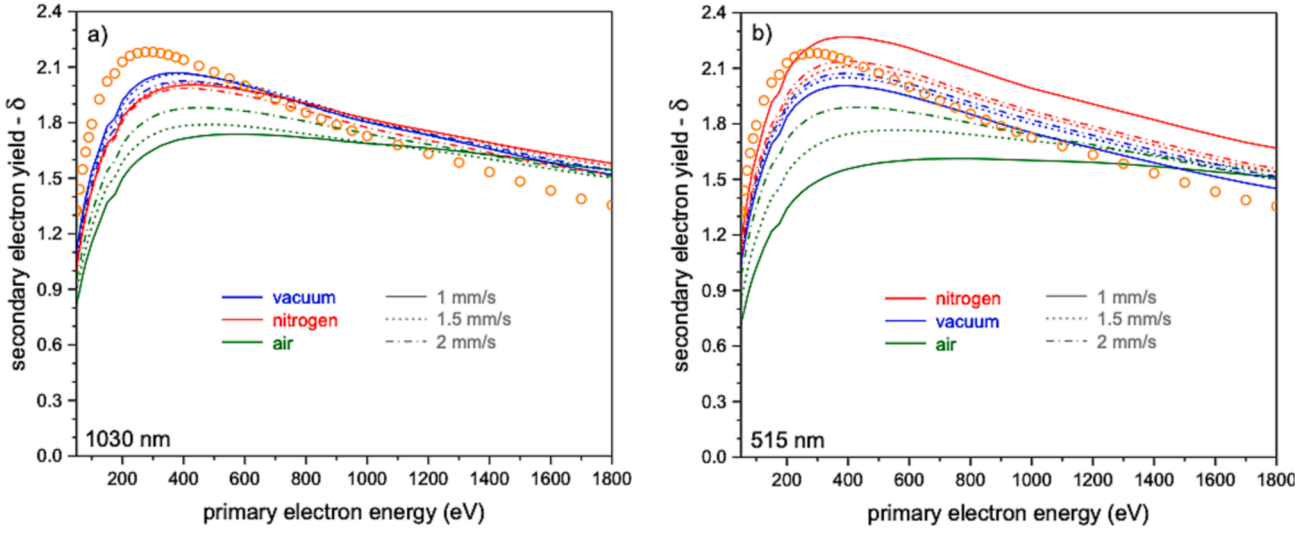

Fig. 7. Secondary electron yield in dependence of primary electron energy for Cu samples processed with (a) 1030 nm and (b) 515 nm laser light and varying scanning speed. The orange circles represent the curve for degreased Cu prior laser treatment. (For interpretation of the references to colour in this figure legend, the reader is referred to the web version of this article.)

Fig. 5 (c)). While the surface chemical composition – one factor that influences the SEY – is found independent of the scanning speed within the investigated range, the observed variation of surface topography is solely affecting the SEY reduction. The lowest δ_{max} values were obtained for 515 nm in air at 1 mm/s (at the lowest presented accumulated fluence), while a lower treatment speed, and hence higher number of pulses, inevitably led to enhanced particle redeposition at the surface. The samples that were processed in vacuum and nitrogen did not exhibit a clear trend of topography changes, and consequently the SEY also did not vary strongly. Laser processing in air is more efficient to form LIPSS with high aspect ratio (see Table 3), which is beneficial for SEY reduction [8].

The variation of the SEY upon exposure to electrons (*conditioning*) is an important characteristic for materials in particle accelerators, as it influences the electron cloud intensity during continuous operation [57], and is critical for the effectiveness of electron scrubbing campaigns [58,59]. We therefore characterized three selected samples with different initial δ_{max}, after stepwise exposure to an increasing dose of 250 eV electrons using a flood gun, and tracked the variation of the SEY in dependence of the electron dose. The variation of δ_{max} up to a dose of approximately 10^{-2}C/mm^2 is shown in Fig. 8. The results confirmed the tendency of our earlier study that LIPSS on Cu allow a conditioning of the surface to obtain $\delta_{max} < 1$, equivalent to a regime where no electron multiplication can occur. It is also evident that the initial SEY variation is important to qualify whether this condition can be reached. For the case of the sample treated in N_2, for which the initial δ_{max} was>2, the SEY maximum stabilized at 1.04 at a dose $> 2 \times 10^{-2}$C. To obtain a significant improvement for a surface treatment campaign in larger particle accelerator installations, ideally the electron-cloud threshold, which is typically between 1.05 and 1.25 [60] needs to be reached at electron doses $\leq 5 \times 10^{-4}$C/mm^2.

3.4. Electromagnetic characterization.

For characterization of the surface resistivity, a perturbative technique is implemented, which allows to measure small changes in the resonance of a dielectrically loaded cavity. We performed resistivity measurements of a LIPSS sample processed in ambient air using $\lambda \approx$ 1030 nm and $v = 2$ mm/s, which was placed in a cylindrical copper cavity loaded with a dielectric single crystal sapphire puck, having 3.5 mm radius and 3.5 mm height. The design consists in an *ad hoc* modification of a Hakki-Coleman dielectric resonator [39].

In our measurement setup, the unknown resistivity (ρ) of LIPSS is derived from the measurement of the dielectric resonator quality factor (Q) variations inserting the sample inside the cavity with respect to a reference material (OFE copper). To increase the system sensitivity, we measured a number of known materials (molybdenum, niobium and zirconium) with the same dimensions ($10 \times 10 \times 1$ mm^3) of the sample under study in order to extract a calibration curve [61]. For each known material, we measured the quality factor and the resonance frequency of the TE_{011} mode operating approximately at 15 GHz, repeatedly mounting and dismounting the sample to minimize the errors due to the sample position and the coupling with antennas. Both influence the total measurement error and require attention and time. The electric field of the TE_{011} mode has only the azimuthal component. Its field lines and current distributions follow circular paths on the sample surface with the field being mainly concentrated in the sample center. This behavior assures that contribution to the total losses and to the Q due to the side, top and bottom walls are negligible.

Simulation analyses were in addition performed using an EM code (CST Studio Suite® - SIMULIA by Dassault Systèmes), aimed at studying the electromagnetic behavior of the cavity without and with the dielectric and for the extrapolation of the expected calibration curve with the different conductivities of the available materials. All the measured unloaded Q values extracted in post-processing are compared to the unloaded Q_{ref} of an OFE copper sample used as a reference ($Q_{ref} = 3.4 \times 10^3$, $\rho_{ref} = 17.2$ nΩ·m). Fig. 9 shows the normalized quality factor (Q/Q_{ref}) as a function of the resistivity ratio (ρ/ρ_{copper}) for all the materials, including the LIPSS sample created in air, with the corresponding error bars. From the measurements of known materials, we extracted the calibration curve, $\frac{Q}{Q_{ref}} = \frac{a+b}{a\sqrt{\frac{\rho}{\rho_{ref}}}+b}$, where a and b are constants proportional to the losses in the sample and in the rest of the cavity, respectively. It is displayed as a continues red line in Fig. 9.

Resorting to the calibration curve and to the measured Q value, the LIPSS surface resistance R_s was evaluated from the resistivity ($\rho_{LIPSS} =$ 95.2 nΩ m), yielding a value of 76 mΩ. The increase in the surface resistance with respect to copper value (estimated $R_s = 32$ mΩ) was expected due to the dimensions of the "wavy" profile larger than the skin depth of both the copper, roughly 0.5 μm at the test frequency, and of the LIPSS sample, roughly 1.25 μm with the calculated conductivity. This

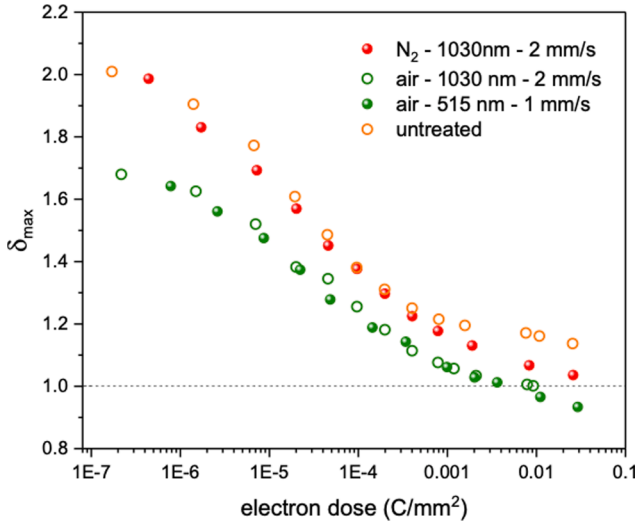

Fig. 8. Variation of the SEY maximum of degreased Cu (orange circles) in comparison with selected laser treated samples with LIPSS upon irradiation with 250 eV electrons in UHV as a function of accumulated dose. (For interpretation of the references to colour in this figure legend, the reader is referred to the web version of this article.)

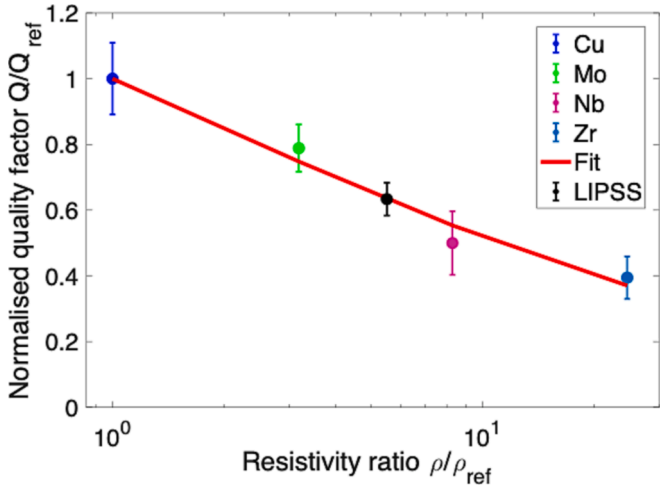

Fig. 9. Normalized quality factor (Q/Q_{ref}) as a function of the resistivity ratio (ρ/ρ_{ref}) for Cu, Mo, Nb, Zr and LIPSS. Copper is taken as reference. The calibration curve is shown as a continuous red line. (For interpretation of the references to colour in this figure legend, the reader is referred to the web version of this article.)

behavior can be linked to the longer path traveled by circular surface currents on the sample crossing orthogonally the LIPSS channel for half of their path [62]. Our results can be compared with measurements performed on different laser-structured surfaces at lower frequency, 7.8 GHz, and room temperature [63], where R_s varies between 78 mΩ and 140 mΩ, and at 9.1 GHz and low temperatures, where R_s varies between 10 mΩ and 60 mΩ as a function of scanning lines distance and temperature [64]. Our data are comparable with those coming from other laser-structured surfaces considering that R_s increases with the square-rooted frequency, with temperature and that in the LIPSS case the scanning lines are closer. The value of the measured surface resistance does not appear to be critical for present accelerators [62,64].

Further measurements on new samples are foreseen to study the impact of different LIPPS channel patterns on surface resistance considering their orientation with respect to the surface currents linked to the cavity TE_{011} mode.

4. Conclusions

We investigated the influence of the ambient conditions, treatment speed and wavelength during the femtosecond laser processing of copper to form LIPSS on the surface to study the possible implementation of these tailored treatments in a real element of accelerator of the order of several hundreds of meters. Differences in the LIPSS periodicity and depth as well as depth of large-scale channels are found, which have direct influence on the surface topography and aspect ratio. The treatment in air creates deeper structures with preferred tendency to particle redeposition. For all three environments (air, vacuum, and nitrogen), the surface composition shows distinct differences, regardless of scanning speed and laser wavelength. While the laser-treatment in air does not induce a further oxidation of the Cu_2O-like surface but rather a removal of surface adsorbates, the processing in vacuum or nitrogen creates a partially metallic surface. The morphological and chemical changes explain well the differences in the secondary electron yield of the modified Cu surfaces. The analyses revealed that laser-processing of Cu in ambient air, at low beam scanning velocity (1 mm/s) and at 515 nm laser wavelength allows the lowest possible SEY maximum of 1.6. At the same time, these parameters represent the onset of particle redeposition and limit the SEY maximum of particle-free LIPSS surfaces to 1.6–1.7. At higher fluences, a further reduction of the SEY is obtained due to surface roughness enhancement via nanoparticle uptake. After electron-induced surface conditioning, an SEY maximum below 1 is obtained for samples that have been processed in air. The influence of the topography modulation on the surface resistance, and consequently on the resistive wall impedance, was also evaluated and found to agree with measurements performed on other laser treated samples. The results of these studies open the real possibility to apply LIPSS treatment to larger elements to be installed in accelerators.

Declaration of Competing Interest

The authors declare that they have no known competing financial interests or personal relationships that could have appeared to influence the work reported in this paper.

Data availability

Data will be made available on request.

Acknowledgement

The authors dedicate this article to prof. Vittorio Giorgio Vaccaro (INFN-Na, UNINA), recently passed away, for all the fruitful stimuli, for his endless curiosity and humanity.The authors are grateful to Mauro Taborelli (CERN) for manuscript reading and fruitful discussions. This work was conducted under the aegis of National Institute of Nuclear Physics (INFN), ARYA experiment, and CERN, collaboration KN4963/TE Addendum no.14 and its Amendments no. 1 to Agreement KN3083 CERN-INFN. J. JJ N. acknowledges the support by the Italian Ministry of University and Research (MUR) under PON "Ricerca e Innovazione" 2014-2020 (Azione IV.4, Asse IV – DM 1062/2021, FSE REACT-EU). M. H. acknowledges the financial support from China Scholarship Council for her PhD grant. S. A. and R. F. acknowledge the PRIN 2020 project CONQUEST funded by the Italian MUR (Prot. 2020JZ5N9M). C. A. and M. V. acknowledge either the support by the Italian MUR under the PRIN "Predicting and controlling the fate of bio-molecules driven by extreme ultra-violet radiation" (Prot. - 20173B72NB) and the support by the Campania Region under the POR FSE 2014-2020 ASSE III, 2022-2023 (CUP B69J19000500007).

Appendix A. Supplementary material

Supplementary data to this article can be found online at https://doi.org/10.1016/j.apsusc.2023.156908.

References

[1] O. Domínguez, K. Li, G. Arduini, E. Métral, G. Rumolo, F. Zimmermann, H. M. Cuna, First electron-cloud studies at the Large Hadron Collider, Phys. Rev. Spec. Top. - Accel. Beams. 16 (2013), https://doi.org/10.1103/PhysRevSTAB.16.011003.
[2] R. Cimino, T. Demma, Electron cloud in accelerators, Int. J. Mod. Phys. A. 29 (2014), https://doi.org/10.1142/S0217751X14300233.
[3] F. Zimmermann, Review of single bunch instabilities driven by an electron cloud, Phys. Rev. Spec. Top. - Accel. Beams. 7 (2004) 121–156, https://doi.org/10.1103/PhysRevSTAB.7.124801.
[4] G. Rumolo, F. Ruggiero, F. Zimmermann, Simulation of the electron-cloud build up and its consequences on heat load, beam stability, and diagnostics, Phys. Rev. Spec. Top. - Accel. Beams. 4 (2001), https://doi.org/10.1103/PhysRevSTAB.4.012801.
[5] V. Shiltsev, F. Zimmermann, Modern and future colliders, Rev. Mod. Phys. 93 (2021).
[6] P. Costa Pinto, S. Calatroni, H. Neupert, D. Letant-Delrieux, P. Edwards, P. Chiggiato, M. Taborelli, W. Vollenberg, C. Yin-Vallgren, J.L. Colaux, S. Lucas, Carbon coatings with low secondary electron yield, Vacuum. 98 (2013) 29–36, https://doi.org/10.1016/J.VACUUM.2013.03.001.
[7] M. Nishiwaki, S. Kato, Influence of electron irradiation and heating on secondary electron yields from non-evaporable getter films observed with in situ x-ray photoelectron spectroscopy, J. Vac. Sci. Technol. A Vacuum, Surfaces, Film. 25 (2007) 675–679, https://doi.org/10.1116/1.2738491.
[8] M. Pivi, F.K. King, R.E. Kirby, T.O. Raubenheimer, G. Stupakov, F. Le Pimpec, Sharp reduction of the secondary electron emission yield from grooved surfaces, J. Appl. Phys. 104 (2008), 104904, https://doi.org/10.1063/1.3021149.
[9] M. Himmerlich, D.A. Zanin, M. Taborelli, A.R. Granadeiro Costa, P. Costa Pinto, L. Lain Amador, W. Vollenberg, A. Baris, E. Garcia-Tabares Valdivieso, A.T. Perez Fontenla, S. Wackerow, A. Abdolvand, Efficient Combination of Surface Texturing and Functional Coating for Very Low Secondary Electron Yield Surfaces and Rough Nonevaporable Getter Films., Adv. Mater. Interfaces. (2022). https://doi.org/https://doi.org/10.1002/admi.202201671.
[10] R. Valizadeh, O.B. Malyshev, S. Wang, S.A. Zolotovskaya, W.A. Gillespie, A. Abdolvand, Low secondary electron yield engineered surface for electron cloud mitigation, Appl. Phys. Lett. 105 (2014), 231605, https://doi.org/10.1063/1.4902993.
[11] S. Calatroni, E. Garcia-Tabares Valdivieso, H. Neupert, V. Nistor, A.T. Perez Fontenla, M. Taborelli, P. Chiggiato, O. Malyshev, R. Valizadeh, S. Wackerow, S. A. Zolotovskaya, W.A. Gillespie, A. Abdolvand, First accelerator test of vacuum components with laser-engineered surfaces for electron-cloud mitigation, Phys. Rev. Accel. Beams. 20 (2017), 113201, https://doi.org/10.1103/PhysRevAccelBeams.20.113201.
[12] S. Calatroni, E. Garcia-Tabares Valdivieso, A.T. Perez Fontenla, M. Taborelli, H. Neupert, M. Himmerlich, P. Chiggiato, D. Bajek, S. Wackerow, A. Abdolvand, Optimization of the secondary electron yield of laser-structured copper surfaces at room and cryogenic temperature, Phys. Rev. Accel. Beams. 23 (2020), 033101, https://doi.org/10.1103/PhysRevAccelBeams.23.033101.
[13] R. Valizadeh, O.B. Malyshev, S. Wang, T. Sian, M.D. Cropper, N. Sykes, Reduction of secondary electron yield for E-cloud mitigation by laser ablation surface engineering, Appl. Surf. Sci. 404 (2017) 370–379, https://doi.org/10.1016/j.apsusc.2017.02.013.
[14] D. Bajek, S. Wackerow, D.A. Zanin, L. Baudin, K. Bogdanowicz, E.G.T. Valdivieso, S. Calatroni, B. Di Girolamo, M. Sitko, M. Himmerlich, M. Taborelli, P. Chiggiato, A. Abdolvand, Role of surface microgeometries on electron escape probability and secondary electron yield of metal surfaces, Sci. Rep. 10 (2020), https://doi.org/10.1038/s41598-019-57160-w.
[15] Z.K. Lorenz Pierre, H. Marcel, B. Elena, B. Karolina, T. Mauro, Secondary electron yield reduction of copper after 355 nm ultrashort pulse laser ablation, Lasers Manuf. Mater. Process. 9 (2022) 135–150.

[16] J. Jj Nivas, M. Valadan, M. Salvatore, R. Fittipaldi, M. Himmerlich, M. Rimoldi, A. Passarelli, E. Allahyari, S.L. Oscurato, A. Vecchione, C. Altucci, S. Amoruso, A. Andreone, S. Calatroni, M.R. Masullo, Secondary electron yield reduction by femtosecond pulse laser-induced periodic surface structuring, Surfaces and Interfaces. 25 (2021), 101179, https://doi.org/10.1016/j.surfin.2021.101179.

[17] J. Bonse, S. Hohm, S.V. Kirner, A. Rosenfeld, J. Kruger, Laser-induced periodic surface structures-a scientific evergreen, IEEE J. Sel. Top. Quantum Electron. 23 (2017) 9000615, https://doi.org/10.1109/JSTQE.2016.2614183.

[18] A.Y. Vorobyev, C. Guo, Direct femtosecond laser surface nano/microstructuring and its applications, Laser Photonics Rev. 7 (2013) 385–407, https://doi.org/10.1002/lpor.201200017.

[19] D.S. Correa, J.M.P. Almeida, G.F.B. Almeida, M.R. Cardoso, L. De Boni, C.R. Mendonça, Ultrafast Laser Pulses for Structuring Materials at Micro/Nano Scale: From Waveguides to Superhydrophobic Surfaces, Photonics 2017, Vol. 4, Page 8. 4 (2017) 8. https://doi.org/10.3390/PHOTONICS4010008.

[20] E. Allahyari, J.J.J. Nivas, S.L. Oscurato, M. Salvatore, G. Ausanio, A. Vecchione, R. Fittipaldi, P. Maddalena, R. Bruzzese, S. Amoruso, Laser surface texturing of copper and variation of the wetting response with the laser pulse fluence, Appl. Surf. Sci. 470 (2019) 817–824, https://doi.org/10.1016/J.APSUSC.2018.11.202.

[21] J. Jj Nivas, K.K. Anoop, R. Bruzzese, R. Philip, S. Amoruso, Direct femtosecond laser surface structuring of crystalline silicon at 400 nm, Appl. Phys. Lett. 112 (2018), 121601, https://doi.org/10.1063/1.5011134.

[22] J. Jj Nivas, E. Allahyari, F. Cardano, A. Rubano, R. Fittipaldi, A. Vecchione, D. Paparo, L. Marrucci, R. Bruzzese, S. Amoruso, Surface structures with unconventional patterns and shapes generated by femtosecond structured light fields, Sci. Rep. 8 (2018) 13613, https://doi.org/10.1038/s41598-018-31768-w.

[23] E. Allahyari, J.J.J. Nivas, M. Valadan, R. Fittipaldi, A. Vecchione, L. Parlato, R. Bruzzese, C. Altucci, S. Amoruso, Plume shielding effects in ultrafast laser surface texturing of silicon at high repetition rate in air, Appl. Surf. Sci. 488 (2019) 128–133, https://doi.org/10.1016/j.apsusc.2019.05.219.

[24] E. Allahyari, J.J.J. Nivas, G. Avallone, M. Valadan, M. Singh, V. Granata, C. Cirillo, A. Vecchione, R. Bruzzese, C. Altucci, S. Amoruso, Femtosecond laser surface irradiation of silicon in air: pulse repetition rate influence on crater features and surface texture, Opt. Laser Technol. 126 (2020), 106073, https://doi.org/10.1016/j.optlastec.2020.106073.

[25] M. Hu, J.J.J. Nivas, M. Valadan, R. Fittipaldi, A. Vecchione, R. Bruzzese, C. Altucci, S. Amoruso, Ultrafast laser surface irradiation of silicon: effects of repetition rate in vacuum and air, Appl. Surf. Sci. 606 (2022), 154869, https://doi.org/10.1016/J.APSUSC.2022.154869.

[26] J. Jj Nivas, Z. Song, R. Fittipaldi, A. Vecchione, R. Bruzzese, S. Amoruso, Direct ultrashort laser surface structuring of silicon in air and vacuum at 1055 nm, Appl. Surf. Sci. 417 (2017) 149–154, https://doi.org/10.1016/j.apsusc.2017.03.158.

[27] M. Migliorati, E. Belli, M. Zobov, Impact of the resistive wall impedance on beam dynamics in the future circular e+e- collider, Phys. Rev. Accel. Beams. 21 (2018), 041001, https://doi.org/10.1103/PhysRevAccelBeams.21.041001.

[28] Y. Shobuda, Y.H. Chin, Resistive-wall impedances of a thin non-evaporable getter coating on a conductive chamber, Prog. Theor. Exp. Phys. 2017 (2017) 123–124, https://doi.org/10.1093/PTEP/PTX167.

[29] X.Q. Chen, G.Y. Zhu, F. Caspers, J.C. Yang, J.X. Wu, G.D. Shen, J. Liu, J.W. Xia, Y. Zhang, S. Ruan, G. Wang, L.P.Y. Yao, F.C. Cai, H.R. Ren, Q.Y. Kong, Y.Z. Gao, Transverse broadband impedance reduction techniques in a heavy ion accelerator, Phys. Rev. Accel. Beams. 23 (2020), 034402, https://doi.org/10.1103/PhysRevAccelBeams.23.034402.

[30] G. Rumolo, H. Bartosik, E. Belli, P. Dijkstal, G. Iadarola, K. Li, L. Mether, A. Romano, M. Schenk, F. Zimmermann, Electron Cloud Effects at the LHC and LHC Injectors, IPAC 2017 Eighth Int. Part. Accel. Conf. (2017) 30–36. https://doi.org/10.18429/JACOW-IPAC2017-MOZA1.

[31] J.M. Liu, Simple technique for measurements of pulsed Gaussian-beam spot sizes, Opt. Lett. 7 (1982) 196–198, https://doi.org/10.1364/OL.7.000196.

[32] P. Gecys, E. Markauskas, M. Gedvilas, G. Raciukaitis, I. Repins, C. Beall, Ultrashort pulsed laser induced material lift-off processing of CZTSe thin-film solar cells, Sol. Energy. 102 (2014) 82–90, https://doi.org/10.1016/J.SOLENER.2014.01.013.

[33] J. Krüger, W. Kautek, Ultrashort Pulse Laser Interaction with Dielectrics and Polymers, in: T. Lippert (Ed.), Polym. Light Adv. Polym. Sci. 168, Springer, Berlin, Heidelberg, 2004: pp. 247–290. https://doi.org/10.1007/b12683.

[34] D. Bouilly, D. Perez, L.J. Lewis, Damage in materials following ablation by ultrashort laser pulses: A molecular-dynamics study, Phys. Rev. B - Condens. Matter Mater. Phys. 76 (2007), 184119, https://doi.org/10.1103/PhysRevB.76.184119.

[35] C.A. Zuhlke, G.D. Tsibidis, T. Anderson, E. Stratakis, G. Gogos, D.R. Alexander, Investigation of femtosecond laser induced ripple formation on copper for varying incident angle, AIP Adv. 8 (2018), 015212, https://doi.org/10.1063/1.5020029.

[36] A. Passarelli, C. Koral, M.R. Masullo, W. Vollenberg, L.L. Amador, A. Andreone, Sub-THz Waveguide Spectroscopy of Coating Materials for Particle Accelerators, Condens. Matter 2020, Vol. 5, Page 9. 5 (2020) 9. https://doi.org/10.3390/CONDMAT5010009.

[37] J. Krupka, W. Strupinski, N. Kwietniewski, Microwave conductivity of very thin graphene and metal films, J. Nanosci. Nanotechnol. 11 (2011) 3358–3362, https://doi.org/10.1166/JNN.2011.3728.

[38] L. Hao, J. Gallop, S. Goniszewski, O. Shaforost, N. Klein, R. Yakimova, Non-contact method for measurement of the microwave conductivity of graphene, Appl. Phys. Lett. 103 (2013), 123103, https://doi.org/10.1063/1.4821268.

[39] J. Mazierska, Dielectric resonator as a possible standard for characterization of high temperature superconducting films for microwave applications, J. Supercond. 1997 102. 10 (1997) 73–84. https://doi.org/10.1007/BF02763176.

[40] C. Wu, L.V. Zhigilei, Microscopic mechanisms of laser spallation and ablation of metal targets from large-scale molecular dynamics simulations, Appl. Phys. A Mater. Sci. Process. 114 (2014) 11–32, https://doi.org/10.1007/S00339-013-8086-4/FIGURES/8.

[41] A.Y. Vorobyev, C. Guo, Enhanced absorptance of gold following multipulse femtosecond laser ablation, Phys. Rev. B. 72 (2005), 195422, https://doi.org/10.1103/PhysRevB.72.195422.

[42] J. Ghijsen, L.H. Tjeng, J. Van Elp, H. Eskes, J. Westerink, G.A. Sawatzky, M. T. Czyzyk, Electronic structure of Cu 2 O and CuO, Phys. Rev. B. 38 (1988) 11322, https://doi.org/10.1103/PhysRevB.38.11322.

[43] S. Poulston, P.M. Parlett, P. Stone, M. Bowker, Surface oxidation and reduction of CuO and CuzO studied using XPS and XAES, Surf. INTERFACE Anal. 24 (1996) 811–820, https://doi.org/10.1002/(SICI)1096-9918(199611)24:12.

[44] M.C. Biesinger, Advanced analysis of copper X-ray photoelectron spectra, Surf. Interface Anal. 49 (2017) 1325–1334, https://doi.org/10.1002/SIA.6239.

[45] V. Petit, M. Taborelli, D.A. Zanin, M. Himmerlich, H. Neupert, P. Chiggiato, G. Iadarola, Beam-induced surface modifications as a critical source of heat loads in the Large Hadron Collider, Commun. Phys. 2021 41. 4 (2021) 1–10. https://doi.org/10.1038/s42005-021-00698-x.

[46] E. Bez, M. Himmerlich, P. Lorenz, M. Ehrhardt, A.G. Gunn, S. Pfeiffer, M. Rimoldi, M. Taborelli, K. Zimmer, P. Chiggiato, A. Anders, Influence of wavelength and accumulated fluence at picosecond laser-induced surface roughening of copper on secondary electron yield, J. Appl. Phys. 133 (2023), 035303.

[47] S.K. Chawla, B.I. Rickett, N. Sankarraman, J.H. Payer, An X-ray photo-electron spectroscopic investigation of the air-formed film on copper, Corros. Sci. 33 (1992) 1617.

[48] J. Iijima, J.W. Lim, S.H. Hong, S. Suzuki, K. Mimura, M. Isshiki, Native oxidation of ultra high purity Cu bulk and thin films, Appl. Surf. Science. 253 (2006) 2825.

[49] I. Platzman, R. Brener, H. Haick, R. Tannenbaum, Oxidation of polycrystalline copper thin films at ambient conditions, J. Phys. Chem. C. 112 (2008) 1101.

[50] V.S. Levitskii, V.I. Shapovalov, A.E. Komlev, A. V. Zav'yalov, V. V. Vit'ko, A.A. Komlev, E.S. Shutova, Raman spectroscopy of copper oxide films deposited by reactive magnetron sputtering, Tech. Phys. Lett. 41 (2015) 1094–1096. https://doi.org/10.1134/S106378501511022X.

[51] J. Chrzanowski, J.C. Irwin, Raman scattering from single crystals of cupric oxide, Solid State Commun. 70 (1989) 11–14.

[52] M. Rashad, M. Rüsing, G. Berth, K. Lischka, A. Pawlis, CuO and Co3O4 nanoparticles: synthesis, characterizations, and Raman spectroscopy, J. Nanomater. 2013 (2013) 82, https://doi.org/10.1155/2013/714853.

[53] J. Reydellet, M. Balkanski, D. Trivich, Light scattering and infrared absorption in cuprous oxide, Phys. Stat. Sol. B. 52 (1972) 175–185, https://doi.org/10.1002/pssb.2220520120.

[54] B.K. Meyer, A. Polity, D. Reppin, M. Becker, P. Hering, P.J. Klar, T. Sander, C. Reindl, J. Benz, M. Eickhoff, C. Heiliger, M. Heinemann, J. Bläsing, A. Krost, S. Shokovets, C. Müller, C. Ronning, Binary copper oxide semiconductors: From materials towards devices, Phys. Status Solidi B. 249 (2012) 1487–1509, https://doi.org/10.1002/pssb.201248128.

[55] R. Cimino, M. Commisso, D.R. Grosso, T. Demma, V. Baglin, R. Flammini, R. Larciprete, Nature of the decrease of the secondary-electron yield by electron bombardment and its energy dependence, Phys. Rev. Lett. 109 (2012), 064801, https://doi.org/10.1103/PhysRevLett.109.064801.

[56] V. Petit, M. Taborelli, H. Neupert, P. Chiggiato, M. Belhaj, Role of the different chemical components in the conditioning process of air exposed copper surfaces, Phys. Rev. Accel. Beams. 22 (2019), 083101, https://doi.org/10.1103/PhysRevAccelBeams.22.083101.

[57] E. Buratin, V. Baglin, B. Henrist, P. Chiggiato, A. Fasoli, Electron flux and pressure dynamic in the LHC vacuum pilot sector as a function of beam parameters and beam pipe properties, Phys. Rev. Accel. Beams. 23 (2020), 114802, https://doi.org/10.1103/PhysRevAccelBeams.23.114802.

[58] O. Bruning, F. Caspers, I.R. Collins, O. Grobner, B. Henrist, N. Hilleret, J. M. Laurent, M. Morvillo, M. Pivi, F. Ruggiero, X. Zhang, Electron cloud and beam scrubbing in the LHC, Proc. IEEE Part. Accel. Conf. 4 (1999) 2629–2631, https://doi.org/10.1109/PAC.1999.792885.

[59] Y. Suetsugu, K. Shibata, T. Ishibashi, K. Kanazawa, M. Shirai, S. Terui, H. Hisamatsu, First commissioning of the SuperKEKB vacuum system, Phys. Rev. Accel. Beams. 19 (2016), 121001, https://doi.org/10.1103/PhysRevAccelBeams.19.121001.

[60] G. Iadarola, Electron cloud studies for CERN particle accelerators and simulation code development, CERN-THESIS-2014-047_2, Università degli Studi di Napoli Federico II, Napoli, Italy & European Organization for Nuclear Research, Geneva, Switzerland, https://cds.cern.ch/record/1705520?ln=de, n.d. https://cds.cern.ch/record/1705520?ln=de.

[61] A. Carlotta, A. David, A.A. Sergey, B. Adrienn, B. Alessandro, B. Nicolò, C. Sergio, C. Federico, C. Fritz, G.T.V. Elisa, G.V. Jorge, K. Adnan, M. Alessio, M. Elias, R. Stefano, S. Benoit, T. Mauro, V. Wilhelmus, Resistivity Characterization of Molybdenum-Coated Graphite-Based Substrates for High-Luminosity LHC Collimators, Coatings 2020, Vol. 10, Page 361. 10 (2020) 361. https://doi.org/10.3390/COATINGS10040361.

[62] Sergio Calatroni,* Marco Arzeo, Sarah Aull, Marcel Himmerlich, Pedro Costa Pinto, A.A. Wilhelmus Vollenberg, Beniamino Di Girolamo, Paul Cruikshank, Paolo Chiggiato, David Bajek, Stefan Wackerow, Cryogenic surface resistance of copper: Investigation of the impact of surface treatments for secondary electron yield

reduction, Phys. Rev. Accel. Beams. 22 (2019) 063101. https://doi.org/10.1103/PhysRevAccelBeams.22.063101.

[63] N.S. R. Valizadeh, O.B. Malyshev, S. Wang, T. Sian, L. Gurran,P. Goudket,M.D. Cropper, Low secondary electron yield of laser treated surfaces of copper, aluminium and stainless steel, in: IPAC 2016,7th Int. Part. Accel. Conf., Busan, Korea, 2016: pp. 1089–1092.

[64] P. Krkotić, S. Calatroni, X. Granados, J. Gutierrez, A. Hannah, RF Characterisation of New Coatings for Future Circular Collider Beam Screens, 12th Int. Part. Accel. Conf. (2021) 2454–2456. https://doi.org/10.18429/JACoW-IPAC2021-TUPAB399.